

Shear responses of $[\bar{1}10]$ -tilt $\{115\}/\{111\}$ asymmetric tilt grain boundaries in fcc metals by atomistic simulations

Liang Wan^{1,2} and Ju Li^{1,2,3}

¹ Center for Advancing Materials Performance from Nanoscale, State Key Laboratory for Mechanical Behavior of Materials, Xi'an Jiaotong University, Xi'an 710049, People's Republic of China

² Frontier Institute of Science and Technology, Xi'an Jiaotong University, Xi'an 710049, People's Republic of China

³ Department of Nuclear Science and Engineering and Department of Materials Science and Engineering, Massachusetts Institute of Technology, Cambridge, Massachusetts 02139, USA

E-mail: liangwan5@gmail.com and juli@mit.edu


Received 30 November 2012, in final form 17 April 2013

Published 31 May 2013

Online at stacks.iop.org/MSMSE/21/055013

Abstract

The shear response of the $\Sigma 3$ $[\bar{1}10]$ -tilt $(\bar{1}\bar{1}5)/(111)$ and $\Sigma 9$ $[\bar{1}10]$ -tilt $(115)/(111)$ asymmetric tilt grain boundaries (GBs) in fcc metals Cu and Al has been studied by atomistic simulation methods with the embedded atom method interatomic potentials and with a bicrystal model. It is found that the structure of the GBs studied can be well described by the coincidence site lattice (CSL) theory. Shear of these GBs at room temperature along eight different directions within the GB plane shows that these two types of GBs can transform between each other by the formation of a coherent twin boundary. The structure transformation of the GBs can also take the form of GB sliding, GB sliding–migration coupled motion, GB faceting, GB θ R structure formation, etc, depending on the shear directions adopted and the material involved (Cu or Al). The detailed structure transformation mechanisms have been analyzed with the aid of the CSL–DSC (displacement shift complete) theory. Several structure transformation paths adherent to these two types of GBs have been identified for the activation of the GB sliding–migration coupled motion. It is concluded that, although CSL–DSC theory can be applied to describe the sliding–migration coupled motion of the GBs studied, some other effects such as the shear direction within the GB plane and the bonding characteristics of the materials should also play a significant role in the shear response of these GBs.

 Online supplementary data available from stacks.iop.org/MSMSE/21/055013/mmedia

(Some figures may appear in colour only in the online journal)

1. Introduction

Grain boundaries (GBs) are an important aspect of microstructure in most materials and play a significant role in their mechanical behavior [1]. In metallic nanocrystalline or ultrafine-grained materials, GB-mediated plasticity can be a major deformation mechanism for the straining of these kinds of materials [2]. A comprehensive understanding of the shear response of individual GBs from the atomic scale can thus be useful for obtaining a clear picture of the mechanical behavior of these materials [3]. Generally, this requires a thorough knowledge of the ‘structure–mechanical behavior’ relationship for all kinds of GBs. However, since there are five variables for characterizing the geometry orientation of a single GB [1], it would be intractable to make an exhaustive exploration in this five-dimensional materials parameter space [4, 5]. To better achieve this goal, it is usually helpful to start from a well-established structure model of GBs such as the coincidence site lattice (CSL) theory, and to choose GBs with low Σ values and with low indexed boundary planes from preliminary studies [6–17].

On the other hand, experiments show that grain growth can happen in the mechanical loading of nanocrystalline metals at ambient or even lower temperatures [18–26], and it can be partially attributed to the shear stress-induced GB migration behavior [25]. This kind of GB migration behavior is quite different from the GB migration phenomena that occurs during recrystallization processes of metal polycrystals at relatively higher temperatures [27]. However, the mechanism for shear-stress-induced GB migration behavior is still unclear.

Within the CSL framework, it is predicted that some low Σ GBs can slide and migrate by the motion of GB DSC (displacement shift complete) dislocations [1, 28–31]. However, the CSL–DSC theory is a pure crystallographic description of the GB motion. Whether this theory can be applied to describe the shear response of a particular Σ GB (and perhaps its vicinal boundaries) with regard to the embodying materials and external loading conditions, or if the CSL theory can even describe the structure of a specific Σ GB (and also its vicinal boundaries) in a real material are open questions.

In this work, the $\Sigma 3$ $[\bar{1} 1 0]$ -tilt $(\bar{1} \bar{1} 5)/(1 1 1)$ and $\Sigma 9$ $[\bar{1} 1 0]$ -tilt $(1 1 5)/(1 1 1)$ asymmetric tilt GBs in fcc metals Cu and Al were selected for study. These two types of GBs (hereafter termed $\Sigma 3$ GB and $\Sigma 9$ GB for short, respectively) can relate to each other in that the $\Sigma 9$ GB can be obtained by a 180° rotation of the upper crystal of the $\Sigma 3$ GB around the normal of the GB plane while keeping the lower crystal fixed, and vice versa. The atomistic simulation methods including the energy minimization technique and the molecular dynamics (MD) simulation method were employed for a detailed investigation of the GB structure and its shear response. By exerting shear stresses with different directions along the GB plane, we can identify the shear direction-dependent structure transformation behavior of the GBs. The detailed structure transformation mechanisms were analyzed with the aid of the CSL–DSC theory. This is followed by a discussion of the applicability of the CSL–DSC theory for the GBs studied. A summary of the results is given at the end.

2. Model and computational method

The bicrystal model used in this work is illustrated in figure 1(a). For each type of GB, two orientations of the bicrystals (C1 and C2) were introduced to facilitate the application of shear strain with different shear directions parallel to the GB plane. The specific lattice orientations

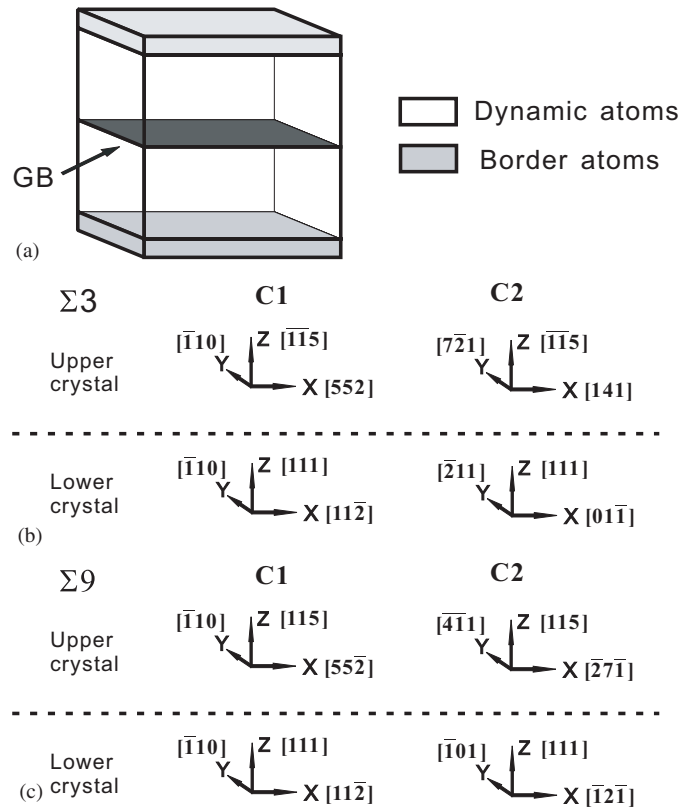


Figure 1. (a) Geometry of the simulation cell and the bicrystal model used in this work. The two orientations of bicrystals (C1 and C2) for the $\Sigma 3$ and $\Sigma 9$ GBs selected are illustrated in (b) and (c) respectively.

Table 1. Dimensions of the initial simulation cells used in this work for all the bicrystals studied. C1 and C2 are the two orientations of bicrystals as illustrated in figure 1. N_x , N_y and N_z represent the number of repeating orthorhombic CSL unit cells inherent to the corresponding orientations of bicrystals in the x -, y - and z - directions, respectively. $L_x \times L_y \times L_z$ stands for the actual sizes of the simulation cells. Lattice constants of 3.615 Å and 4.05 Å have been used for Cu and Al, respectively. N_{atoms} is the total number of atoms in the bicrystal model.

GB-orientation	$N_x \times N_y \times N_z$	$(L_x \times L_y \times L_z)_{\text{Cu}}/\text{Å}^3$	$(L_x \times L_y \times L_z)_{\text{Al}}/\text{Å}^3$	N_{atoms}
$\Sigma 3$ -C1	$6 \times 22 \times 18$	$159.4 \times 112.5 \times 338.1$	$178.6 \times 126.0 \times 378.8$	510, 048
$\Sigma 3$ -C2	$6 \times 6 \times 18$	$92.0 \times 159.4 \times 338.1$	$103.1 \times 178.6 \times 378.8$	417, 312
$\Sigma 9$ -C1	$6 \times 22 \times 18$	$159.4 \times 112.5 \times 338.1$	$178.6 \times 126.0 \times 378.8$	510, 048
$\Sigma 9$ -C2	$6 \times 6 \times 18$	$159.4 \times 92.0 \times 338.1$	$178.6 \times 103.1 \times 378.8$	417, 312

of the upper and lower crystals for each bicrystal orientation of both the $\Sigma 3$ and $\Sigma 9$ GBs are given in figures 1(b) and (c), respectively. The dimensions of the initial simulation cells are given in table 1.

Periodic boundary conditions were applied along the x - and y -directions. A free and a damping boundary schemes were used along the z -direction for the energy minimization

procedure and MD simulations, respectively. In the damping boundary scheme, two slabs along the z -axis at the top and bottom of the simulation cell were designed to give the border region (see figure 1(a)). The thickness of each border slab is around four times the cutoff distance of the interatomic potentials. All the simulations were performed with the LAMMPS code [32].

To obtain the equilibrium structure of GBs, an energy minimization procedure with a standard conjugate-gradient algorithm was performed on a set of initial trial GB structures. The trial GB structures are distinguished by their in-plane rigid body translation vectors within the GB plane. Since the range of unique in-plane rigid body translation vectors is defined by the cell of non-identical displacements (CNID), which in turn can be related to the unit cell of CSL on the GB plane [1], a 10×10 grid of points was generated by dividing the unit cell of CSL on the GB plane to give a uniform sampling of the in-plane translations. The optimized structures obtained were then subjected to an MD annealing procedure to bring them to the equilibrium states at desired temperatures and zero stress.

The shear processes were simulated by the MD method. An integration time step of 2.0 fs was adopted throughout the MD simulations. The Melchionna modified [33] Nosé–Hoover dynamics was applied on the inner atoms between the border slabs for the control of the temperature and stress state of the bicrystals. For atoms belonging to the border slabs, the z -axis component of their coordinates was scaled uniformly according to the length variation of the simulation cell in the z -direction. Meanwhile, the motions of these atoms within the x – y plane were constrained by the Langevin dynamics. The damping coefficient in the Langevin dynamics was chosen such that the traverse waves propagating along the z -axis can attenuate as quickly as possible. The stress and temperature were calculated on the dynamic atoms between the two border slabs. The stress tensor was calculated by the standard Virial expression [34].

Shear strain was applied by deforming the entire model system as a whole. The shear directions were aligned with the x - or y -axis of the simulation cell. The stress components in dimensions other than the shear direction were set to zero to allow the relaxation of bicrystals in these dimensions. Eight shear directions which correspond to the positive and negative directions of the x - and y -axes shown in figure 1 were studied for each GB. The shear strain was calculated by measuring the variation of the shape of the simulation cell. A constant strain rate of $1 \times 10^8 \text{ s}^{-1}$ was used for all the straining simulations. The strain rate is several orders higher than that usually used in experiments. This gap is generally due to the intrinsic limit of the MD method employed.

The EAM-type interatomic potentials fitted by Mishin and co-workers for Cu [35] and Al [36] were used in the atomistic model. These potentials were well tested and were demonstrated to give a good evaluation of a variety of material properties, including the elastic constants, phonon frequencies, thermal expansion, the intrinsic stacking fault energy, the coherent twin boundary energy, etc [35, 36].

The common neighbor analysis (CNA) technique [37] was used to identify the defect structures in the bicrystals. It gives a classification of all the atoms by their local crystallinity. For fcc metals, three categories of atoms were distinguished: atoms of fcc structural order, atoms of hcp structural order, and atoms of other structural order. Within this scheme, for an fcc matrix, a single layer of hcp atoms represents a twin boundary, two adjacent hcp atom layers manifest an intrinsic stacking fault, and two hcp atom layers with a sandwiched fcc atom layer represent an extrinsic stacking fault. The visualization tool AtomEye [38] was used in this work to produce illustrations of defect structures of bicrystals.

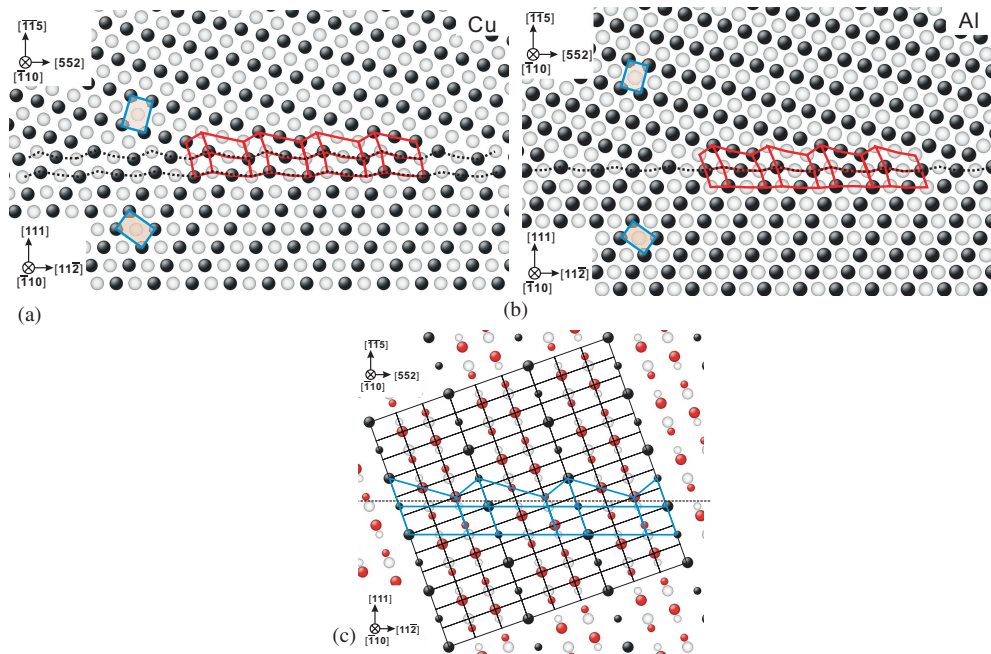


Figure 2. The optimized structures of the $\Sigma 3$ $[\bar{1} 1 0]$ -tilt $(\bar{1} \bar{1} 5)/(1 1 1)$ asymmetric tilt GB for Cu (a) and Al (b) obtained by the energy minimization procedure and subsequent MD annealing at 300 K and zero stress. Black and white spheres correspond to the two alternating $(\bar{2} 2 0)$ lattice planes. (c) is the dichromatic pattern of the $\Sigma 3$ $[\bar{1} 1 0]$ -tilt $(\bar{1} \bar{1} 5)/(1 1 1)$ asymmetric tilt GB in fcc crystals. Red spheres represent the lattice sites of the upper crystal. White spheres represent the lattice sites of the lower crystal. The black spheres are coincidence sites. The fine grid gives the DSC lattice. Spheres of two different sizes correspond to the two alternating $(\bar{2} 2 0)$ lattice planes. The boundary plane is marked by the dashed line.

3. Results

3.1. GB structure and energy

Figures 2(a) and (b) give the optimized GB structures of the $\Sigma 3$ $[\bar{1} 1 0]$ -tilt $(\bar{1} \bar{1} 5)/(1 1 1)$ asymmetric tilt GB for Cu and Al, respectively. The optimized GB structures were obtained from the energy minimization procedure and subsequent MD annealing at 300 K and zero stress. By comparing the optimized GB structures with the dichromatic pattern of the $\Sigma 3$ $[\bar{1} 1 0]$ -tilt $(\bar{1} \bar{1} 5)/(1 1 1)$ asymmetric tilt GB as shown in figure 2(c), it can be seen that the optimized GB structures for both Cu and Al agree quite well with the CSL description. However, as is indicated by the dotted lines in figures 2(a) and (b), the uppermost $(1 1 1)$ layers of the lower crystal become wrinkled in order to give a good match with the surface (the $(\bar{1} \bar{1} 5)$ planes) of the upper crystal. It can also be seen that the wrinkling behavior is more salient in Cu than in Al.

Similar conclusion can also be reached for the $\Sigma 9$ $[\bar{1} 1 0]$ -tilt $(1 1 5)/(1 1 1)$ asymmetric tilt GB. Figures 3(a) and (b) give the optimized GB structures of the $\Sigma 9$ $[\bar{1} 1 0]$ -tilt $(1 1 5)/(1 1 1)$ asymmetric tilt GB for Cu and Al, respectively. The dichromatic pattern for the $\Sigma 9$ $[\bar{1} 1 0]$ -tilt $(1 1 5)/(1 1 1)$ asymmetric tilt GB is illustrated in figure 3(c). It can be seen that the optimized GB structures obtained for both Cu and Al also agree pretty well with the CSL description. Although less salient as compared with the $\Sigma 3$ $[\bar{1} 1 0]$ -tilt $(\bar{1} \bar{1} 5)/(1 1 1)$ asymmetric tilt GB,

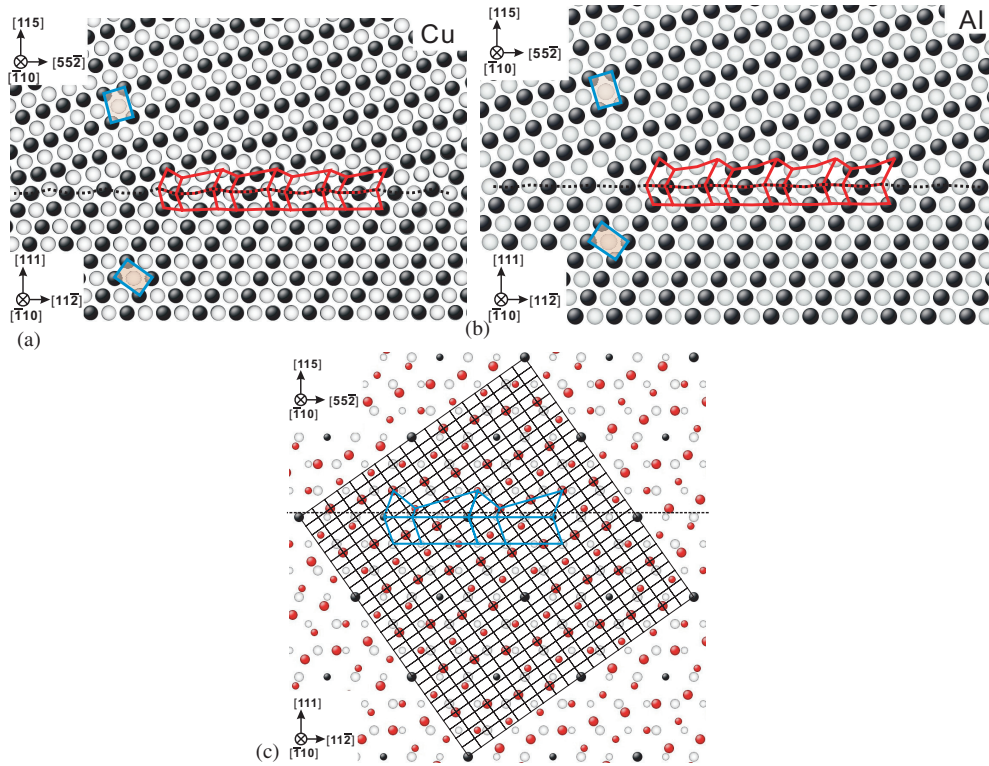


Figure 3. The optimized structures of the $\Sigma 9$ $[\bar{1} 1 0]$ -tilt (1 1 5)/(1 1 1) asymmetric tilt GB for Cu (a) and Al (b) obtained by the energy minimization procedure and subsequent MD annealing at 300 K and zero stress. Black and white spheres correspond to the two alternating $(\bar{2} 2 0)$ lattice planes. (c) is the dichromatic pattern of the $\Sigma 9$ $[\bar{1} 1 0]$ -tilt (1 1 5)/(1 1 1) asymmetric tilt GB in fcc crystals. Red spheres represent the lattice sites of the upper crystal. White spheres represent the lattice sites of the lower crystal. The black spheres are coincidence sites. The fine grid gives the DSC lattice. Spheres of two different sizes correspond to the two alternating $(\bar{2} 2 0)$ lattice planes. The boundary plane is marked by the dashed line.

the wrinkling of the uppermost (1 1 1) layers of the lower crystal can also be recognized (see the dotted lines in figures 3(a) and (b)).

The energies of the GBs at 300 K have also been calculated. It is found that, the energies of these two types of GBs within the same material are nearly the same as each other. For Cu, $E_{\text{gb}}^{\Sigma 3}(300 \text{ K}) = E_{\text{gb}}^{\Sigma 9}(300 \text{ K}) = 600.2 \text{ mJ m}^{-2}$. And for Al, $E_{\text{gb}}^{\Sigma 3}(300 \text{ K}) = E_{\text{gb}}^{\Sigma 9}(300 \text{ K}) = 239.6 \text{ mJ m}^{-2}$. This can be well understood by the fact that, for the $\Sigma 3$ GB and the $\Sigma 9$ GB studied here, figures 2 and 3 show that there is a mirror symmetry relation between the upper crystals of these two types of GBs while the lower crystals resemble each other. The mirror plane is normal to $[1 1 \bar{2}]$ of the lower crystals here. It should be noted that the GB structures and energies of the $\Sigma 3$ GB for both Cu and Al obtained here also agree well with a previous atomistic simulation result [39].

3.2. Shear response of the $\Sigma 3$ $[\bar{1} 1 0]$ -tilt $(\bar{1} \bar{1} 5)/(1 1 1)$ asymmetric tilt GB at room temperature

Figure 4 shows the stress–strain curves for shear of the $\Sigma 3$ $[\bar{1} 1 0]$ -tilt $(\bar{1} \bar{1} 5)/(1 1 1)$ asymmetric tilt GB in both Cu ((a) and (b)) and Al ((c) and (d)) along the eight directions within the GB

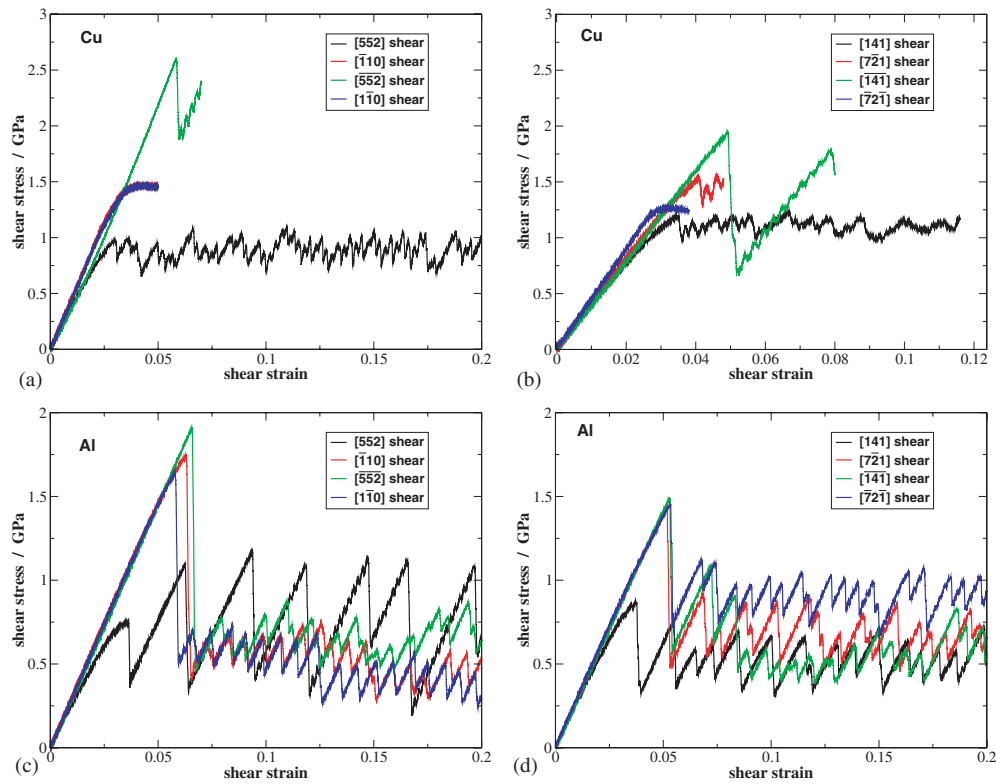


Figure 4. Stress–strain curves for shear of the $\Sigma 3$ $[\bar{1} 1 0]$ -tilt $(\bar{1} \bar{1} 5)/(1 1 1)$ asymmetric tilt GB in Cu ((a) and (b)) and Al ((c) and (d)) bicrystals along the eight directions within the GB plane. The shear directions are given by the lattice directions with reference to the upper crystals (see figure 1(b)). Shear simulations were performed at 300 K and with a constant strain rate of $1 \times 10^8 \text{ s}^{-1}$. The separation of curves for the same material into two groups (i.e. (a) and (b) for Cu, (c) and (d) for Al) is merely for the clarity of the plots.

plane at 300 K. For each shear simulation, the bicrystal was loaded to a total strain of 0.20 along the shear direction. For some shear processes, GB migration or lattice dislocation emission from GB can happen. The migrated GB or emitted lattice dislocations can hit the border of the bicrystal model early before the straining processes were finished. In such cases, the stress–strain curves were then cut off to get rid of the trailing part which is an artifact of the model size effect.

It can be seen that the stress–strain curves are quite different to each other for shear of the same GB along different directions. This is a reflection of a strong shear direction-dependent structure transformation behavior of the shear response of the GB. For a further analysis of the ‘structure–mechanical behavior’ relationship of the GBs, snapshots of atomic configurations are captured periodically during the shear simulations. Figures 5 and 6 give the snapshots of atomic configurations at the final steps of the straining processes for shear of the $\Sigma 3$ $[\bar{1} 1 0]$ -tilt $(\bar{1} \bar{1} 5)/(1 1 1)$ asymmetric tilt GB in Cu and Al bicrystals, respectively. For a clear demonstration of the structure evolution processes, movies corresponding to the shear processes are also provided as the online supplementary materials associated with this paper (stacks.iop.org/MSMSE/21/055013/mmedia) [44].

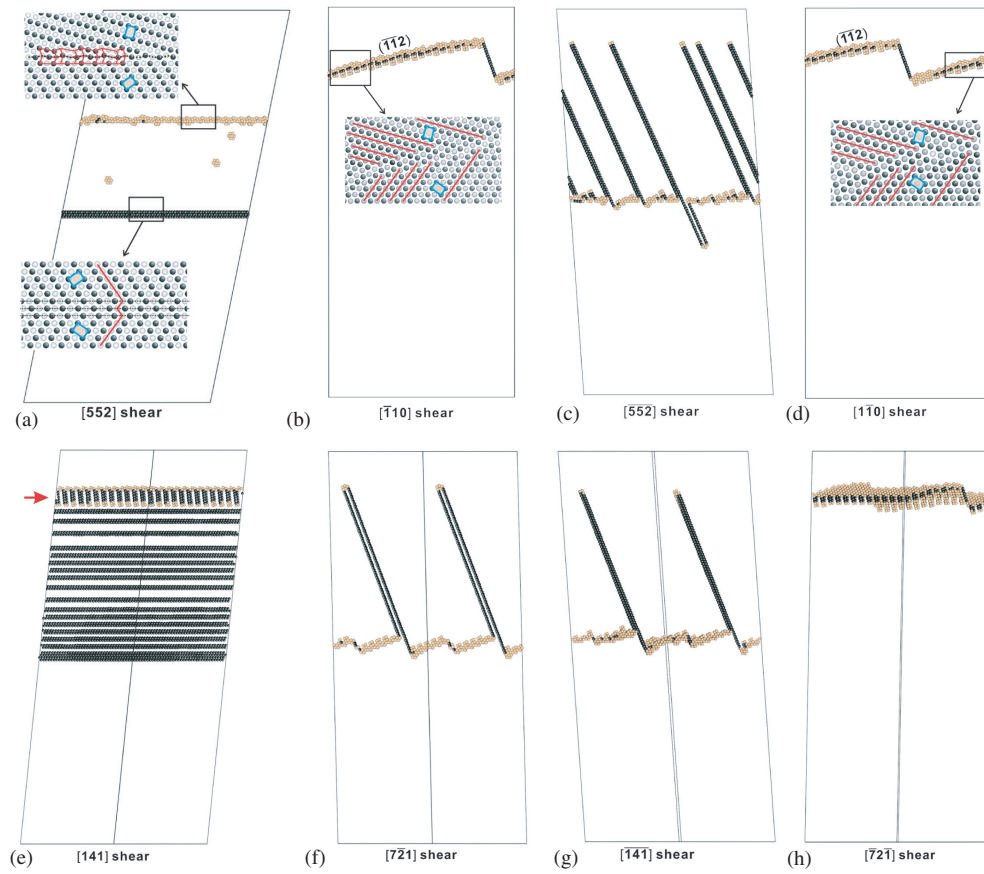


Figure 5. Snapshots of atomic configurations captured at the final steps of the straining processes (the end points on the stress–strain curves in figures 4(a) and (b)) for shear of the Cu bicrystals with the $\Sigma 3$ $[1\ 1\ 0]$ -tilt $(\bar{1}\ \bar{1}\ 5)/(1\ 1\ 1)$ asymmetric tilt GB. All the view directions are along the tilt axis $[\bar{1}\ 1\ 0]$. Only the atoms between the two border slabs which do not have the fcc structural order are displayed. Atoms with HCP structural order are colored dark, while atoms of other structural order are colored light yellow. The insets in (a), (b) and (d) are the enlarged view of the atomic configurations marked by the rectangles. The color scheme used in the insets is the same as that in figure 2(a).

3.2.1. Cu. For shear of the Cu bicrystals with the $\Sigma 3$ $[\bar{1}\ 1\ 0]$ -tilt $(\bar{1}\ \bar{1}\ 5)/(1\ 1\ 1)$ asymmetric tilt GB along all the directions except the $[\bar{5}\ \bar{5}\ \bar{2}]$, $[7\ \bar{2}\ 1]$ and $[\bar{1}\ 4\ \bar{1}]$, the GB can migrate to the upper crystal (see figures 5 and panels (c), (f) and (g)). For shear along $[\bar{1}\ 1\ 0]$, $[1\ \bar{1}\ 0]$ and $[\bar{7}\ 2\ \bar{1}]$, the GB can facet into a $\Sigma 3$ coherent twin boundary joint with a $\Sigma 3$ $(\bar{1}\ \bar{1}\ 2)$ symmetric tilt GB during the shear processes (see figures 5(b), (d) and (h), and also the movie files in the online supplementary data). The faceted GB can migrate away with much less shear strain applied (see the red and blue curves in figure 4(a) and the blue curve in figure 4(b)). Although faceting of flat GBs during annealing of bulk polycrystals at relatively higher temperatures can be generally understood by the free energy decrease of the faceting transformation [1], faceting of GBs by shear stress under athermal loading conditions as demonstrated here can be different. This will be discussed later in the discussion section.

For shear along $[1\ 4\ 1]$, figure 5(e) shows that stacking faults can be generated and left behind while the GB is migrating forward. A detailed analysis (see the movie file in the online

supplementary data (stacks.iop.org/MSMSE/21/055013/mmedia) indicates that the GB first dissociated with stacking faults extending into the lower crystal in the initial straining stage. The dissociated GB forms the so-called 9R structure [45–48] adjoining to the GB as indicated by the red arrow in figure 5(e). It seems that the boundary between the 9R structure and the lower crystal can act as the site for the heterogeneous nucleation of stacking faults parallel to the GB plane under shear stress.

For shear of the $\Sigma 3$ $[\bar{1} 1 0]$ -tilt $(\bar{1} \bar{1} 5)/(1 1 1)$ asymmetric tilt GB in Cu along $[5 5 2]$, a twin structure (see the lower inset in figure 5(a)) was firstly formed in the lower crystal by the similar GB dissociation mechanism (see the movie file in the online supplementary data). The GB then transformed into the $\Sigma 9$ $[\bar{1} 1 0]$ -tilt $(1 1 5)/(1 1 1)$ asymmetric tilt GB (see the upper inset in figure 5(a)) due to the symmetry relationship of these two types of boundaries as mentioned before. Further shear straining along this direction will make the transformed GB migrate to the upper crystal. Several point defects (see figure 5(a)) can be left behind the migrated GB in this shear process.

On the other hand, for shear of the Cu bicrystals along $[\bar{5} \bar{5} \bar{2}]$, $[7 \bar{2} 1]$ and $[\bar{1} \bar{4} \bar{1}]$, figures 5(c), (f) and (g) show that the GB just emits lattice partial dislocations without migration. The GB itself then became more disordered or nano-faceted. The peak shear stresses in these shear processes are relatively higher as compared with the peak shear stresses of the other shear processes (see figures 4(a) and (b)). This probably implies that the critical stress for the emission of the partial dislocations by shear of the GB should be much higher than that for the initiation of the GB splitting or GB faceting–migration motion. It should also be noted that, shear of the $\Sigma 3$ $[\bar{1} 1 0]$ -tilt $(\bar{1} \bar{1} 5)/(1 1 1)$ asymmetric tilt GB in Cu along $[5 5 2]$ has the lowest peak shear stress (around 1.0 GPa, see the black curve in figure 4(a)) among all the shear directions selected in this study.

3.2.2. *Al.* By comparing figure 6 with figure 5 (and also the curves in figure 4), it can be seen that, even with the same type of GB, the Al bicrystals behave very differently with the Cu bicrystals. No lattice dislocation emission event can be identified. In most cases, the GB can migrate upward or downward, and the migration distance can vary depending on the different shear directions adopted in the shear processes. Faceting of the GB can also be verified for shear of the Al bicrystal along $[\bar{1} 1 0]$ and $[1 \bar{1} 0]$ (see figures 6(b) and (d) and the movie files in the online supplementary data). But the detailed faceting processes and the faceted planes are somewhat different with that in Cu bicrystals. Instead of the formation of two $\Sigma 3$ symmetric tilt boundaries, two other $\Sigma 3$ asymmetric tilt GBs are formed in these two shear processes for Al.

For shear of the Al bicrystal along $[5 5 2]$ (figure 6(a)), detailed analysis shows that a twin boundary was initially formed by the similar GB dissociation mechanism as mentioned above in the Cu cases (see the movie file in the online supplementary data). And the original $\Sigma 3$ $[\bar{1} 1 0]$ -tilt $(\bar{1} \bar{1} 5)/(1 1 1)$ asymmetric tilt GB then transformed into the $\Sigma 9$ $[\bar{1} 1 0]$ -tilt $(1 1 5)/(1 1 1)$ asymmetric tilt GB (see the inset in figure 6(a)). However, in the following straining process, the transformed GB stays almost unchanged. It is the sliding–migration of the newly formed twin boundary into the lower crystal that relaxes the elastic shear stress in the bicrystal (see the large drops of shear stress on the black curve in figure 4(c)).

A salient feature of the straining processes for shear of the $\Sigma 3$ $[\bar{1} 1 0]$ -tilt $(\bar{1} \bar{1} 5)/(1 1 1)$ asymmetric tilt GB in Al is that, an obvious drop of the peak shear stress can be recognized on the stress–strain curves for all the shear directions except $[5 5 2]$ (see figures 4(c) and (d)). It is quite likely that some kinds of GB structure transformations happened in the initial straining stages of the bicrystals, and it gives the first drops of the shear stress on the stress–strain curves in figures 4(c) and (d). The transformed GB then makes the succeeding structure

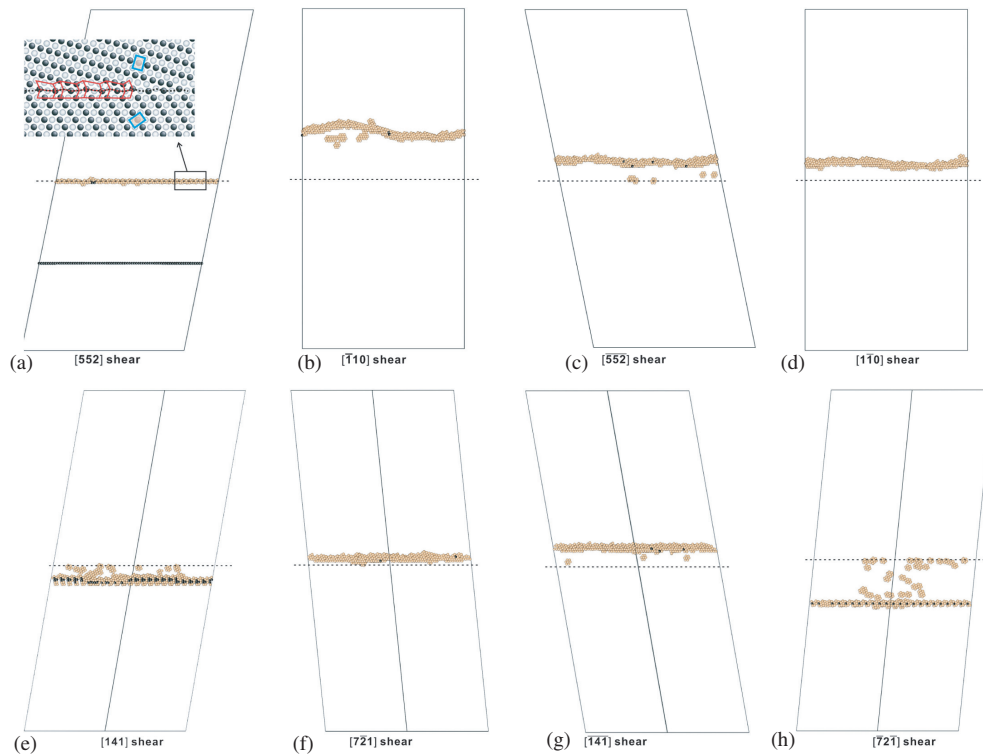


Figure 6. Snapshots of atomic configurations captured at the final steps of the straining processes for shear of the Al bicrystals with the $\Sigma 3$ $[\bar{1}10]$ -tilt $(\bar{1}\bar{1}5)/(111)$ asymmetric tilt GB. All the view directions are along the tilt axis $[\bar{1}10]$. Only the atoms between the two border slabs which do not have the fcc structural order are displayed. Atoms with hcp structural order are colored dark, while atoms of other structural order are colored light yellow. The initial positions of the GB plane are marked by the dashed lines. The inset in (a) is the enlarged view of the atomic configuration marked by the rectangle. The color scheme used in the inset is the same as that in figure 2(b).

transformations by shear of it easier. However, we have not been able to identify for sure the details of these kinds of GB structure transformations in each case. But we emphasize that the GB structure becomes somewhat more disordered (see figures 6(b), (c), (d), (f) and (g)), and point defects can be left behind as the GB migrates (see figures 6(b), (c), (e), (g) and (h)). Such shear-softening response may be akin to shear-rejuvenation of metallic glasses [49] where structural changes (injection of ‘free volume’) makes subsequent shearing easier.

3.3. Shear response of the $\Sigma 9$ $[\bar{1}10]$ -tilt $(115)/(111)$ asymmetric tilt GB at room temperature

Figures 7(a)–(d) show the room temperature stress–strain curves for shear of the $\Sigma 9$ $[\bar{1}10]$ -tilt $(115)/(111)$ asymmetric tilt GB in Cu and Al, respectively. A total shear strain of 0.2 is applied for these straining simulations as well. It should be mentioned that the stress–strain curve for shear of the Cu bicrystal along $[\bar{4}\bar{1}1]$ (the red curve in figure 7(b)) has been truncated for the same reason as those in figure 4.

It can be seen from these curves that the shear response of $\Sigma 9$ $[\bar{1}10]$ -tilt $(115)/(111)$ asymmetric tilt GB in Cu and Al is also strongly shear direction dependent. Meanwhile, many of the curves display a ‘stick-slip’ behavior [12] of the shear response.

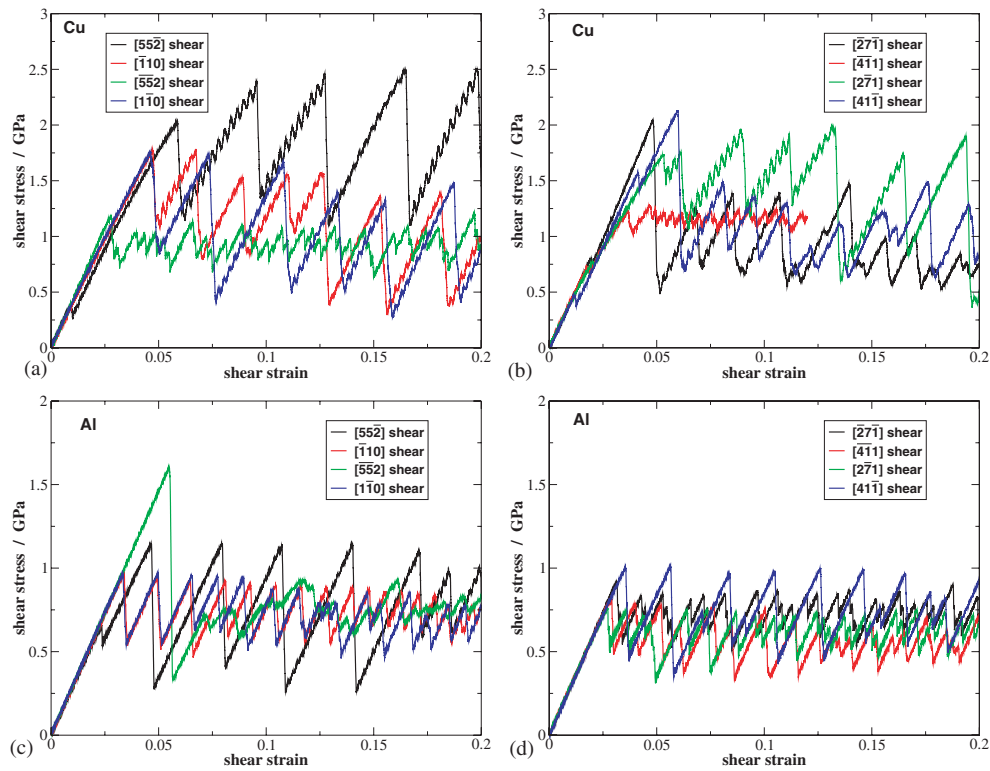


Figure 7. Stress–strain curves for shear of the $\Sigma 9$ $[\bar{1}10]$ -tilt $(115)/(111)$ asymmetric tilt GB in Cu ((a) and (b)) and Al ((c) and (d)) along the eight directions within the GB plane. The shear directions are given by lattice directions with reference to the upper crystals (see figure 1(c)). Straining simulations were performed at 300 K and with a constant strain rate of $1 \times 10^8 \text{ s}^{-1}$. The separation of curves for the same material into two groups (i.e. (a) and (b) for Cu, (c) and (d) for Al) is merely for the clarity of the plots.

To unveil the structure transformation mechanisms underlying the stress–strain behavior of the shear response, snapshots of atomic configurations were also captured periodically during these straining simulations. Figures 8 and 9 give the snapshots of atomic configurations at the final steps of the straining processes for shear of the $\Sigma 9$ $[\bar{1}10]$ -tilt $(115)/(111)$ asymmetric tilt GB in Cu and Al bicrystals, respectively. Movies corresponding to these shear processes are provided as the online supplementary materials associated with this paper as well (stacks.iop.org/MSMSE/21/055013/mmedia) [44].

3.3.1. Cu. For shear of the Cu bicrystals with the $\Sigma 9$ $[\bar{1}10]$ -tilt $(115)/(111)$ asymmetric tilt GB along all the directions except the $[\bar{5}\bar{5}2]$ (figure 8(c)) and $[\bar{2}7\bar{1}]$ (figure 8(e)), a twin boundary was first formed adjacent to the original GB in the lower crystal (see figure 8 and also the movie files in the online supplementary data (stacks.iop.org/MSMSE/21/055013/mmedia)). The mechanism for the formation of the twin boundary here is somewhat different from the GB dissociation mechanism as for shear of the $\Sigma 3$ $[\bar{1}10]$ -tilt $(\bar{1}\bar{1}5)/(111)$ asymmetric tilt GB mentioned above. It seems that a match of the (115) and (111) planes at the interface gives a ‘lock structure’ for displacement of the upper crystal relative to the lower crystal along certain directions (see figure 11 and the discussion there). In this case, the

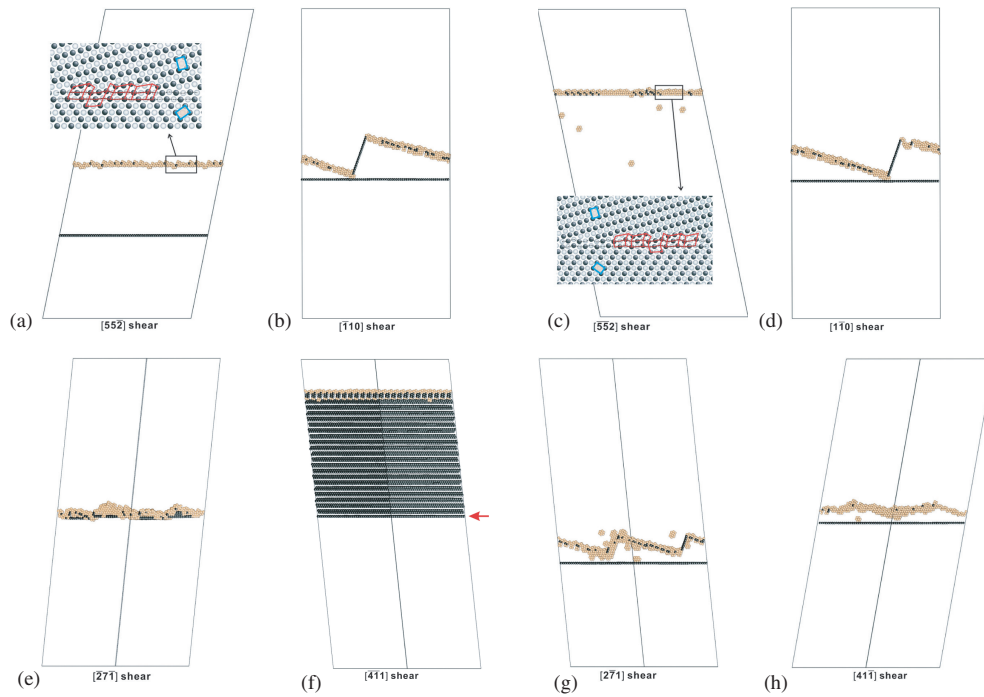


Figure 8. Snapshots of atomic configurations captured at the final steps of the straining processes (the end points on the stress–strain curves in figures 7(a) and (b)) for shear of the Cu bicrystals with the $\Sigma 9$ $[\bar{1} 1 0]$ -tilt $(1 1 5)/(1 1 1)$ asymmetric tilt GB. All the view directions are along the tilt axis $[\bar{1} 1 0]$. Only the atoms between the two border slabs which do not have the fcc structural order are displayed. Atoms with hcp structural order are colored dark, while atoms of other structural order are colored light yellow. The insets in (a), (c) are the enlarged view of the atomic configurations marked by the rectangles. The color scheme used in the insets is the same as that in figure 3(a).

wrinkling of the uppermost $(1 1 1)$ layers of the lower crystal (see figure 3(a)) can possibly assist the inter-layer gliding of the $(1 1 1)$ layers right below the GB. And it thus makes the formation of the twin boundary possible (see the movie files in the online supplementary data).

As is illustrated in the inset of figure 8(a), by the formation of a new twin boundary in the lower crystal, the original $\Sigma 9$ $[\bar{1} 1 0]$ -tilt $(1 1 5)/(1 1 1)$ asymmetric tilt GB then transformed into the $\Sigma 3$ $[\bar{1} 1 0]$ -tilt $(\bar{1} \bar{1} 5)/(1 1 1)$ asymmetric tilt GB. For shear along $[\bar{1} 1 0]$, $[1 \bar{1} 0]$ and $[2 \bar{7} 1]$ (see figures 8(b), (d) and (g) respectively), the transformed GB then faceted in a way very similar to the cases illustrated in figures 5(b) and (d). However, the faceted GB does not migrate for shear along the $[\bar{1} 1 0]$ and $[1 \bar{1} 0]$ in the $\Sigma 9$ GB cases. And for shear along $[2 \bar{7} 1]$, the faceted GB can migrate down along with the twin boundary.

It is worth mentioning that, dissociation of the $\Sigma 9$ $[\bar{1} 1 0]$ -tilt $(1 1 5)/(1 1 1)$ asymmetric tilt GB into a triangular prism bounded by two coherent twin boundaries and a $\Sigma 3$ $(\bar{1} \bar{1} 2)$ symmetric tilt GB has already been observed experimentally in the annealed bulk polycrystal sample of a Cu alloy [50]. The triangular prism observed in that work is quite similar to the ones shown in figures 8(b) and (d). An atomic shuffling mechanism which is different from the GB dissociation mechanism as described above has also been proposed for the formation of the triangular prism [50]. However, considering that the atomic shuffling mechanism implies that there is no shear transformation associated and the transformed $\Sigma 3$ $[\bar{1} 1 0]$ -tilt $(\bar{1} \bar{1} 5)/(1 1 1)$

asymmetric tilt GB will inevitably move upward, we argue that the GB dissociation mechanism by gliding of the (1 1 1) layers right below the GB as described above is more likely to be the one adopted in our cases.

For shear along $[4\bar{1}\bar{1}]$, figure 8(h) shows that the transformed GB can become more disordered by shear of it. It looks like that faceting of the transformed GB can also be recognized (see figure 8(h) and the movie file in the online supplementary data (stacks.iop.org/MSMSE/21/055013/mmedia)). But the faceting behavior is different from those for shear along $[\bar{1}10]$, $[1\bar{1}0]$ and $[2\bar{7}1]$ (figures 8(b), (d) and (g)) in both the faceting process and the faceted planes.

For shear along $[\bar{4}\bar{1}1]$, figure 8(f) shows that the transformed GB migrates upward with stacking faults generated and left behind (the twin boundary formed by the initial dissociation of the original GB is indicated by the red arrow in this figure). This is quite similar to the case for shear of the $\Sigma 3$ $[\bar{1}10]$ -tilt $(\bar{1}\bar{1}5)/(111)$ asymmetric tilt GB in Cu along $[\bar{1}41]$ as shown in figure 5(e). It is also found that the critical stress level for shear of the $\Sigma 9$ $[\bar{1}10]$ -tilt $(115)/(111)$ asymmetric tilt GB along this direction (around 1.1 GPa, see the red curve in figure 7(b)) is nearly the same for shear of the $\Sigma 3$ $[\bar{1}10]$ -tilt $(\bar{1}\bar{1}5)/(111)$ asymmetric tilt GB along $[141]$ (see the black curve in figure 4(b)).

For shear along $[55\bar{2}]$, the transformed GB stays almost unchanged. The twin boundary migrates downward (see figure 8(a) and the movie file in the online supplementary data). It is the sliding–migration of the twin boundary that relaxes the elastic shear stress as illustrated by the black curve in figure 7(a).

For shear of the $\Sigma 9$ $[\bar{1}10]$ -tilt $(115)/(111)$ asymmetric tilt GB in Cu along $[\bar{5}\bar{5}2]$ (figure 8(c)), no splitting of the GB can be identified. The GB just migrates to the upper crystal. The structure of the GB is preserved during migration process as illustrated by the inset in figure 8(c). It also shows that point defects can be left behind the migrating GB. The critical stress level for shear along this direction is the lowest (around 1.0 GPa, see the green curve in figure 7(a)) among all the shear directions studied. This stress level is also quite close to that for shear of the $\Sigma 3$ $[\bar{1}10]$ -tilt $(\bar{1}\bar{1}5)/(111)$ asymmetric tilt GB in Cu along $[552]$ as illustrated by the black curve in figure 4(a). This can be understood by the fact that a split of the $\Sigma 3$ $[\bar{1}10]$ -tilt $(\bar{1}\bar{1}5)/(111)$ asymmetric tilt GB into a twin boundary and the $\Sigma 9$ $[\bar{1}10]$ -tilt $(115)/(111)$ asymmetric tilt GB in that case (see figure 5(a)) makes the succeeding shear process equivalent to that for shear of the $\Sigma 9$ $[\bar{1}10]$ -tilt $(115)/(111)$ asymmetric tilt GB along $[\bar{5}\bar{5}2]$ in this case.

For shear of the $\Sigma 9$ $[\bar{1}10]$ -tilt $(115)/(111)$ asymmetric tilt GB in Cu along $[\bar{2}\bar{7}\bar{1}]$, figure 8(e) shows that the GB becomes more disordered, and it does not migrate. The black curve in figure 7(b) shows that it has a fairly high initial peak shear stress, but follows with a drop of peak stress level in the succeeding straining process. The obvious drop of peak stress levels on both the black curve (shear along $[\bar{2}\bar{7}\bar{1}]$) and the blue curve (shear along $[4\bar{1}\bar{1}]$) in figure 7(b) can perhaps be related to the GB disordering behavior as well.

3.3.2. Al For shear of the Al bicrystal with the $\Sigma 9$ $[\bar{1}10]$ -tilt $(115)/(111)$ asymmetric tilt GB along $[55\bar{2}]$, the GB also splits into a twin boundary migrating downward and a $\Sigma 3$ $[\bar{1}10]$ -tilt $(\bar{1}\bar{1}5)/(111)$ asymmetric tilt GB which stays in its initial position (see figure 9(a) and also the movie file in the online supplementary data). This is very similar to that for shear of the Cu bicrystal with the $\Sigma 9$ $[\bar{1}10]$ -tilt $(115)/(111)$ asymmetric tilt GB along $[55\bar{2}]$ (figure 8(a)), and also similar to the case for shear of the Al bicrystal with the $\Sigma 3$ $[\bar{1}10]$ -tilt $(\bar{1}\bar{1}5)/(111)$ asymmetric tilt GB along $[552]$ (figure 6(a)).

Figure 9 shows that, for shear of the $\Sigma 9$ $[\bar{1}10]$ -tilt $(115)/(111)$ asymmetric tilt GB in Al along other directions, the GB migrates upward or downward without the formation of any

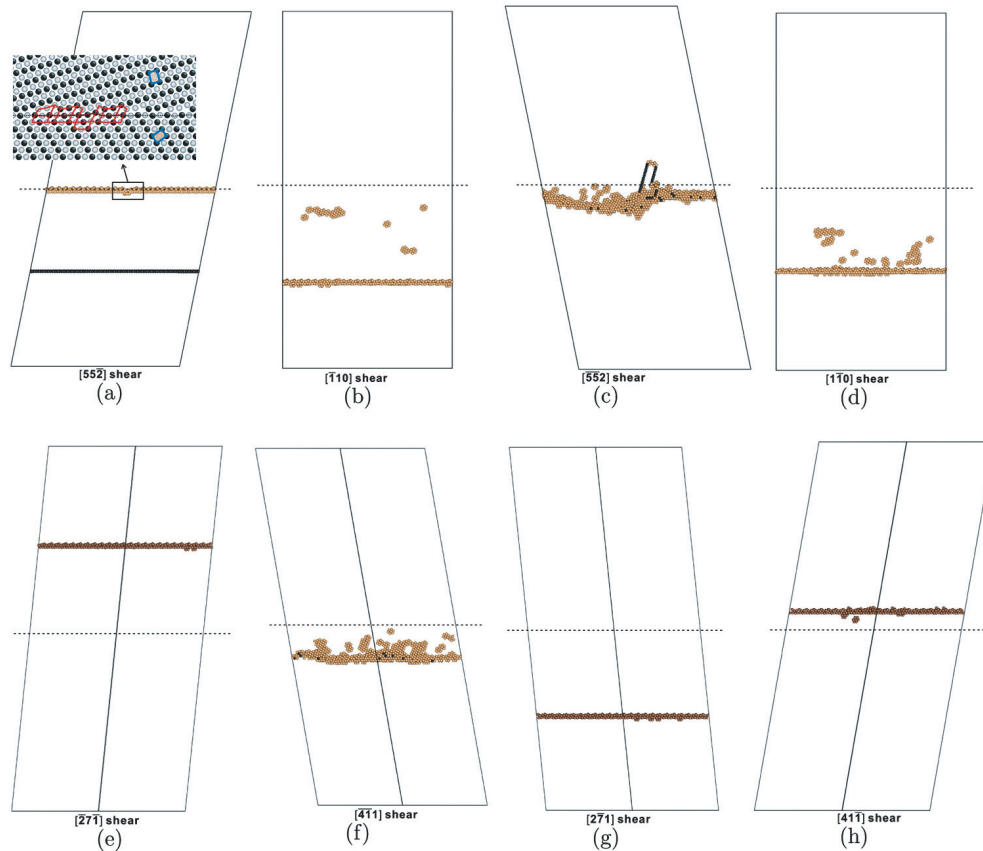


Figure 9. Snapshots of atomic configurations captured at the final steps of the straining processes for shear of the Al bicrystals with the $\Sigma 9$ $[\bar{1}10]$ -tilt $(115)/(111)$ asymmetric tilt GB. All the view directions are along the tilt axis $[\bar{1}10]$. Only the atoms between the two border slabs which do not have the fcc structural order are displayed. Atoms with hcp structural order are colored dark, while atoms of other structural order are colored light yellow. The initial positions of the GB plane are marked by the dashed lines. The inset in (a) is the enlarged view of the atomic configuration marked by the rectangle. The color scheme used in the inset is the same as that in figure 3(b).

new coherent twin boundary, which is quite different from the Cu cases shown in figure 8. The migration distance can be different for shear along different directions. Minor disordering of the GB and formation of point defects in the region swept by the migrating GB can also be identified for shear along some directions (e.g. the shear along $[\bar{4}\bar{1}1]$ as shown in figure 9(f)). However, unlike the cases illustrated in figure 6, the $\Sigma 9$ GB in Al can preserve its initial structure pretty well for shear of it along most directions.

An exception is the shear along $[\bar{5}\bar{5}2]$ which gives a fairly disordered GB structure with complicated faceting behavior and also lattice partial dislocation emission event (see figure 9(c) and the movie file in the online supplementary data (stacks.iop.org/MSMSE/21/055013/mmedia)). It is perhaps this disordering behavior that gives the obvious drop of the peak stress level on the stress–strain curve (the green curve in figure 7(c)), and makes it less regular as compared with other curves in figures 7(c) and (d).

4. Discussion

4.1. Crystallographic analysis of the structure transformations for shear of the $[\bar{1}10]$ -tilt $\{115\}/\{111\}$ asymmetric tilt GBs

We have already demonstrated that the structures of the GBs studied all agree well with the CSL description (see figures 2 and 3). The structure transformation mechanisms underlying the shear response of the GBs can then be analyzed with the aid of the CSL (and the associated DSC lattice) for these two types of GBs [8, 16, 17, 30]. By considering that the Burgers vectors of the GB DSC dislocations (or disconnections) that can be responsible for carrying the GB sliding processes (with or without GB migration) should be as small as possible [51], and with a combined analysis of the simulated results, we can identify the possible atomic structure transformation paths and the associated GB DSC dislocations (or disconnections) that give the shear response of the GBs studied.

Figures 10(a)–(f) give the three possible structure transformation paths for shear of the $\Sigma 3$ $[\bar{1}10]$ -tilt $(\bar{1}\bar{1}5)/(111)$ asymmetric tilt GB in fcc crystals, and figures 11(a)–(d) give the two possible structure transformation paths for shear of the $\Sigma 9$ $[\bar{1}10]$ -tilt $(115)/(111)$ asymmetric tilt GB in fcc crystals. An illustration of the eight shear directions selected within the GB plane can also be found in figures 12(a) and (b) for shear of the $\Sigma 3$ $[\bar{1}10]$ -tilt $(\bar{1}\bar{1}5)/(111)$ and $\Sigma 9$ $[\bar{1}10]$ -tilt $(115)/(111)$ asymmetric tilt GBs, respectively.

As is demonstrated by the green solid arrows in figures 10 and 11, the atoms of the upper crystal in the GB zone (red spheres between the cut planes X1 and X2) can move to the corresponding lattice sites of the lower crystal (white spheres between the cut planes X1 and X2) by shear of the GB along appropriate directions. And the GB can thus migrate upward. In a pure crystallographic sense, the inverse processes can also happen by shear of the GB along the opposite directions, and the GB will thus migrate downward instead. On the other hand, the very same kind of structure transformations can also be accomplished by the replacing the green solid arrows in figures 10 and 11 with their mirror symmetric counterparts (the green dashed arrows in figures 10 and 11). This implies that there is a possible wide range of shear directions within the GB plane that can be adopted to activate the specific structure transformations. Also, this is perhaps one reason why we got many cases of GB sliding–migration coupled motion among the eight shear directions selected for these two types of GBs in Cu and Al.

It should also be noted that, the arrows for a particular structure transformation are not aligned perfectly well within the GB plane, and they may not even parallel to the GB plane as shown in the left panels of figures 10 and 11. This means that shuffling motions of the atoms in the GB zone are required to accomplish the corresponding structure transformations.

Normally, the GB migration is accompanied by the GB sliding, and it gives the GB sliding–migration coupled motion. However, for the structure transformation shown in figures 10(a) and (b), since the atom layer represented by the spheres *I* and *J* may not move, there will be no relative displacement between the upper crystal and lower crystal. The GB will thus migrate upward without apparent shear stress relaxation. This is well demonstrated by the red and blue curves in figure 4(a) and the blue curve in figure 4(b) (see also the corresponding atomic configurations illustrated in figures 5(b), (d) and (h)).

4.2. Applicability of the CSL–DSC theory on the shear response of the $[\bar{1}10]$ -tilt $\{115\}/\{111\}$ asymmetric tilt GBs

If we take the interatomic interactions in real materials (Cu and Al here) into consideration, the structure of the GB can be slightly distorted from the CSL description, and different materials

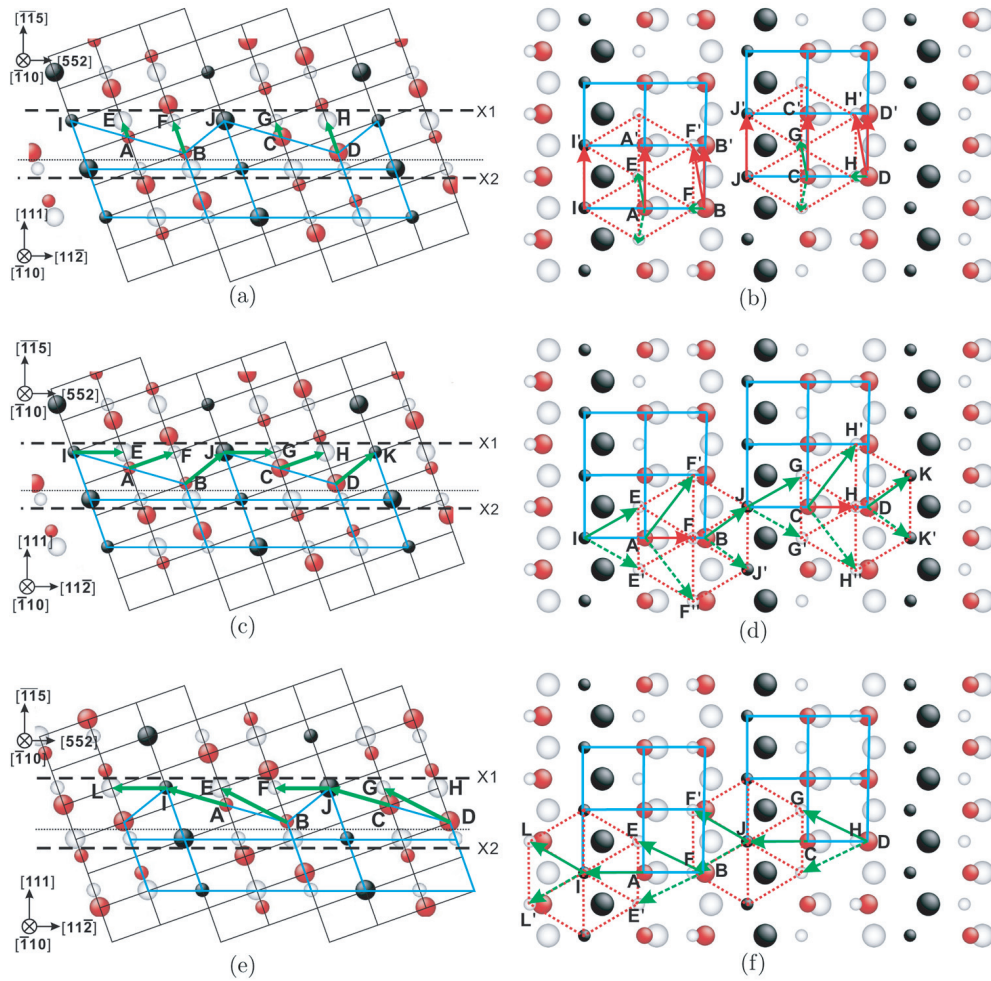


Figure 10. Schematic illustration of the three possible structure transformation paths for shear of the $\Sigma 3$ $[\bar{1}10]$ -tilt $(\bar{1}\bar{1}5)/(111)$ asymmetric tilt GB in fcc crystals. The left panels are the dichromatic pattern of the GB viewed along the tilt axis. The right panels are the projections of the part of lattice between the cut planes X1 and X2 marked in the corresponding left panels viewed along the normal of the GB. Red spheres represent the lattice sites of the upper crystal. White spheres represent the lattice sites of the lower crystal. The black spheres are coincidence sites. In the left panels (a), (c) and (e), spheres of two different sizes correspond to the two alternating (220) lattice planes. The fine grid gives the DSC lattice. And the boundary plane is marked by the dotted line. In the right panels (b), (d) and (f), the size of spheres is used to distinguish lattice sites with different heights along the GB normal, with the smaller spheres sitting over the larger spheres.

can have slightly different GB core structures as shown in figures 2 and 3. Whether or not a particular structure transformation can be activated then depends on the the relative energy barrier heights of the various possible structure transformations. Also, the external conditions such as the shear direction adopted, shear strain rate and the temperature should affect it. The relative barrier heights of the various possible structure transformation paths and their temperature and strain-rate dependence are intimately related to the materials involved. That

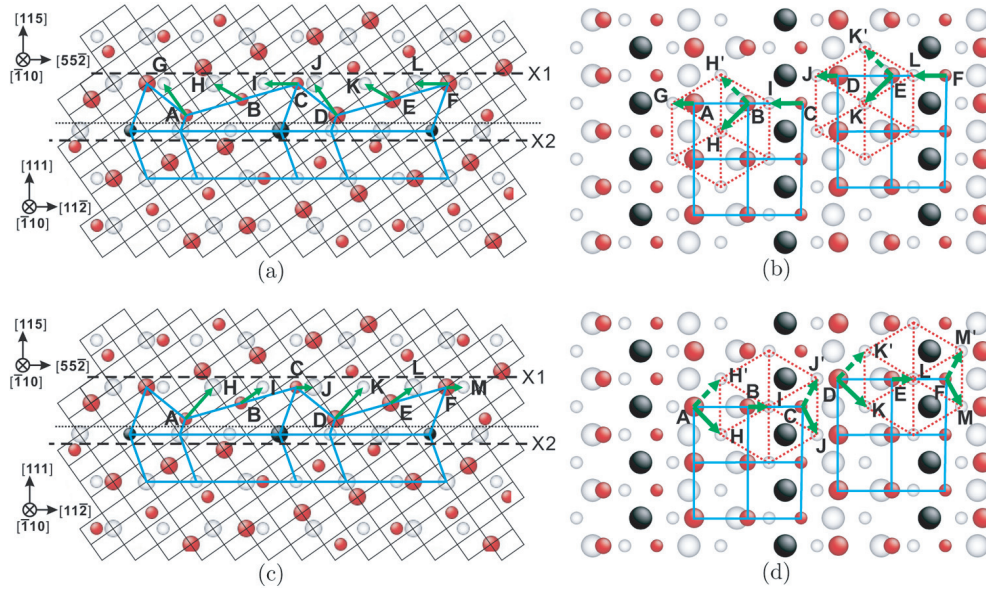


Figure 11. Schematic illustration of the two possible structure transformation paths for shear of the $\Sigma 9$ $[\bar{1}10]$ -tilt $(115)/(111)$ asymmetric tilt GB in fcc crystals. The left panels are the dichromatic pattern of the GB viewed along the tilt axis. The right panels are the projections of the part of lattice between the cut planes X1 and X2 marked in the corresponding left panels viewed along the normal of the GB. Red spheres represent the lattice sites of the upper crystal. White spheres represent the lattice sites of the lower crystal. The black spheres are coincidence sites. In the left panels (a) and (c), spheres of two different sizes correspond to the two alternating (220) lattice planes. The fine grid gives the DSC lattice. And the boundary plane is marked by the dotted line. In the right panels (b) and (d), the size of spheres is used to distinguish lattice sites with different heights along the GB normal, with the smaller spheres sitting over the larger spheres.

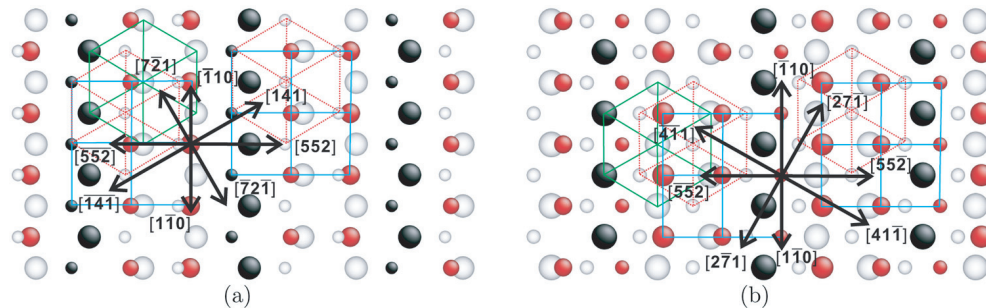


Figure 12. Schematic illustration of the eight selected shear directions along the GB plane for shear of the asymmetric tilt GBs $\Sigma 3$ $[\bar{1}10]$ -tilt $(\bar{1}\bar{1}5)/(111)$ (a) and $\Sigma 9$ $[\bar{1}10]$ -tilt $(115)/(111)$ (b). The same GB views as those in the right panels of figures 10 and 11 are used. The shear directions are given in the crystallographic directions of the upper crystal (see figure 1).

is the reason why the Cu and Al bicrystals with the same type of GB can behave very differently by their shearing along the same direction.

Taking the shear of the $\Sigma 3$ $[\bar{1}10]$ -tilt $(\bar{1}\bar{1}5)/(111)$ asymmetric tilt GB along $[\bar{1}10]$, for example, the structure transformation paths illustrated by the red arrows in figure 10(b) can be adopted as well as the one given by the green arrows in a pure crystallographic sense.

However, the atom layer represented by the largest spheres in this figure (the uppermost (1 1 1) layer of the lower crystal) can act as a strong barrier for the passage of the atom layers represented by the spheres I and B along the paths given by the red arrows \vec{II}' , \vec{BB}' and \vec{BF}' . These kinds of structure transformations were not identified for shear of the Cu bicrystal in this study. On the other hand, for shear of the Al bicrystal with this GB and along $[\bar{1} 1 0]$, the sawtooth like profile of the red curve in figure 4(c) and the atomic configuration shown in figure 6(b) imply that all these structure transformations should have been activated in the shear process.

With the structure transformation path indicated by the green arrows in figure 10(b) adopted, the $\Sigma 3$ $[\bar{1} 1 0]$ -tilt $(\bar{1} \bar{1} 5)/(1 1 1)$ asymmetric tilt GB in Cu will facet and migrate upward without shear transformation accompanied by shearing of it the along $[\bar{1} 1 0]$, $[1 \bar{1} 0]$ and $[\bar{7} 2 \bar{1}]$ (see figures 5(b), (d) and (h), the red and blue curve in figure 4(a), and the blue curve in figure 4(b)). The shear stress induced faceting behavior can be accounted for by the following arguments. With the initial migration of a small GB segment somewhere on the GB plane, a facet embryo will be formed. Although we have not obtained a clear picture, it is likely that the faceted GB (i.e. a $\Sigma 3$ coherent twin boundary joint with a $\Sigma 3$ $(\bar{1} \bar{1} 2)$ symmetric tilt GB) can migrate upward faster than the original flat GB under the shear stress. The faceting process can then proceed smoothly, and it thus gives the structure evolution processes as demonstrated by the movie files in the online supplementary data (stacks.iop.org/MSMSE/21/055013/mmedia).

Another example of the material-dependent structure transformation behavior of the GB is the shear of the $\Sigma 9$ $[\bar{1} 1 0]$ -tilt $(1 1 5)/(1 1 1)$ asymmetric tilt GB along $[\bar{5} \bar{5} 2]$. Figures 11(a) and (b) show that the GB coupling motion with GB migrating upward can happen for shear of this GB along $[\bar{5} \bar{5} 2]$. This is well demonstrated by the atomic configuration shown in figure 8(c) for shear of the Cu bicrystal. However, it should be noted that the transformation requires the atom layer represented by the red sphere B in figures 11(a) and (b) to pass over the layer of atoms represented by the largest white spheres in figure 11(b) (i.e. the uppermost (1 1 1) layer of the lower crystal). The energy barrier for this transformation should be comparatively high for Al, since the atomic configuration shown in figure 9(c) demonstrates that the GB becomes more disordered and it actually migrates downward. The downward migration of the GB by shear of it along $[\bar{5} \bar{5} 2]$ implies that the inverse transformation of that illustrated in figures 11(c) and (d) should have occurred in this shear process.

For a further analysis of the structure transformation mechanisms of the shear processes simulated, we can compare the side displacements of the bicrystals during the shear processes (i.e. the displacement of the upper border relative to the lower border along the direction perpendicular to the shear direction) with the geometry characteristics of the structure transformations as indicated by the crystallographic analysis in figures 10 and 11 and also figure 12. By this sort of analysis and together with the simulated results presented above, the detailed structure transformations involved in the shear processes simulated can then be identified [17]. Here we do not present the somewhat tedious details of the analysis, but only emphasize that the GB sliding–migration coupled motion illustrated by the atomic configurations in figures 5, 6, 8 and 9 can be well interpreted by the structure transformations as shown in figures 10 and 11.

For shear of the GBs with the underlying structure transformations such as those given in figures 10 and 11, a GB DSC dislocation (or disconnection) mechanism is usually suggested [28–31, 51]. The GB disconnection is characterized by its Burgers vector and the associated step height. The Burgers vectors of the GB disconnections for the structure transformations illustrated in figures 10(c)–(f) and figures 11(a)–(d) are $\vec{TE} = \frac{1}{6}[1 4 1]^U = \frac{1}{2}[0 1 \bar{1}]^L$, $\vec{TL} = \frac{1}{6}[\bar{4} \bar{1} \bar{1}]^U = \frac{1}{2}[\bar{1} 0 1]^L$, $\vec{CI} = \frac{1}{18}[\bar{5} \bar{5} 2]^U = \frac{1}{6}[\bar{1} \bar{1} 2]^L$, and $\vec{CJ} = \frac{1}{18}[7 \bar{2} \bar{1}]^U = \frac{1}{6}[2 \bar{1} \bar{1}]^L$,

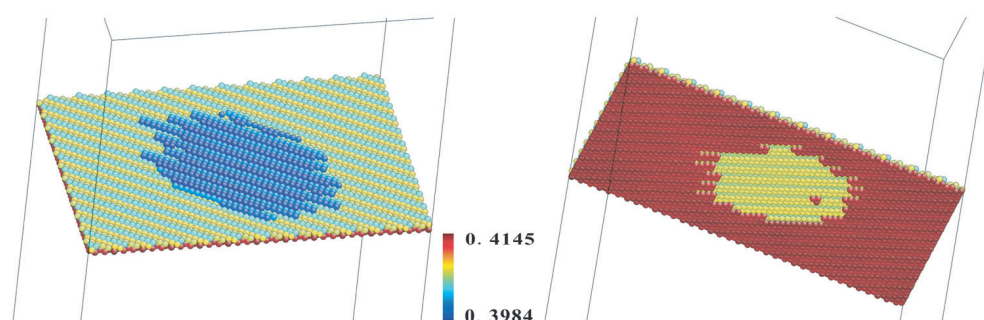


Figure 13. A GB disconnection loop nucleated in shearing of the Al bicrystal with the $\Sigma 9$ $[\bar{1}10]$ -tilt $(115)/(111)$ asymmetric tilt GB along $[\bar{2}7\bar{1}]$. The left and right panels are two views of the GB from the upper and lower sides of the bicrystal, respectively. Atoms displayed are those between the two border slabs which do not have fcc structural order according to the CNA description. The color scale is given as the reduced positions of the atoms along the z -axis (normal to the GB plane).

respectively. Here, the up indexes ' U ' and ' L ' stand for the lattices of the upper crystal and lower crystal, respectively. The step heights of these GB disconnections all equal to the inter-layer distance of the (111) planes.

A homogeneous nucleation and subsequent expansion process of the GB disconnection loops can also be identified for shear of the Al bicrystals where disordering of the GB does not occur (see, for example, shear of the $\Sigma 9$ $[\bar{1}10]$ -tilt $(115)/(111)$ asymmetric tilt GB along $[\bar{2}7\bar{1}]$, $[2\bar{7}1]$ and $[41\bar{1}]$ as illustrated in figures 9(e), (g) and (h)). Figure 13 demonstrates a nucleated GB disconnection loop expanding through the GB plane for shear of the $\Sigma 9$ $[\bar{1}10]$ -tilt $(115)/(111)$ asymmetric tilt GB in Al along $[\bar{2}7\bar{1}]$. A movie of this homogeneous nucleation and subsequent expansion process can be found in the online supplementary materials (stacks.iop.org/MSMSE/21/055013/mmedia).

Last, we would like to mention that the straining simulation is performed with a shear strain rate of $1 \times 10^8 \text{ s}^{-1}$, which is around 10 orders higher than those used in the usual experimental mechanical tests. Figures 4 and 7 show that the lower bounds of the critical shear stresses for the activation of the structure transformations are around 1.0 GPa for Cu and 0.8 GPa for Al. It is hoped that the underlying structure transformation mechanisms should not be significantly changed if the strain rate were reduced to the usual experimental range. An estimation of 20–50% reduction of the critical shear stresses should be reasonable for the activation of these structure transformations in this case [12, 52], not to mention that the heterogeneous nucleation of the GB disconnections with the presence of triple junctions and lattice dislocations can further reduce the critical shear stress.

5. Conclusion

We have studied the room temperature shear response of the $\Sigma 3$ $[\bar{1}10]$ -tilt $(\bar{1}\bar{1}5)/(111)$ and $\Sigma 9$ $[\bar{1}10]$ -tilt $(115)/(111)$ asymmetric tilt GBs in typical fcc metals Cu and Al by atomistic simulation methods with a bicrystal model. It is found that the structure of the GBs studied can be well described by the CSL theory. By shear of the bicrystals along eight different directions within the GB plane at room temperature, various structure transformation behaviors have been identified. It is found that the structure transformation of the GBs under shear can take the form of GB splitting, GB sliding, GB sliding–migration coupled motion, GB faceting, GB 9R

structure formation, etc, depending on the shear directions adopted and the materials involved (Cu or Al).

The underlying structure transformation mechanisms of the shear response of these two types of GBs has been analyzed with the aid of the CSL–DSC theory. Several crystallographically possible atomic structure transformation paths which can lead to the GB migration motion have been recognized. It is found that the GB migration processes with or without GB sliding can be well interpreted by the structure transformation paths proposed. A homogeneous nucleation and subsequent expansion process of the GB dislocation (or disconnection) loops has also been identified for shear of the Al bicrystals along some directions. Based on these results, it can be concluded that, although CSL–DSC theory can be applied to describe sliding–migration coupled motion of the GBs studied, some other effects such as the shear direction within the GB plane and the bond characteristics of the materials should also play a significant role in the shear response of these GBs.

The GBs studied in this work thus add another example of the ‘special’ GBs for which the GB coupling motions realized by the GB DSC dislocations or GB disconnections can occur [16, 17]. It also lends further support to the argument that the GB coupling motions can contribute to the grain coarsening phenomena observed during plastic deformation of nanocrystalline metals loaded at ambient [18–20, 22, 24–26] or even cryogenic temperatures [18, 19].

Acknowledgments

This work is supported by the China Postdoctoral Science Foundation (No. 2012M511995) and National Science Foundation of China (No. 51201127). The authors also thank the 973 Programs of China (2010CB631003, 2012CB619402).

References

- [1] Sutton A P and Balluffi R W 1995 *Interfaces in Crystalline Materials* (Oxford: Clarendon Press)
- [2] Dao M, Lu L, Asaro R J, De Hosson J T M and Ma E 2007 Toward a quantitative understanding of mechanical behavior of nanocrystalline metals *Acta Mater.* **55** 4041–66
- [3] Mishin Y, Asta M and Li J 2010 Atomistic modeling of interfaces and their impact on microstructure and properties *Acta Mater.* **58** 1117–51
- [4] Olmsted D L, Foiles S M and Holm E A 2009 Survey of computed grain boundary properties in face-centered cubic metals: I. Grain boundary energy *Acta Mater.* **57** 3694–703
- [5] Olmsted D L, Holm E A and Foiles S M 2009 Survey of computed grain boundary properties in face centered cubic metals: II. Grain boundary mobility *Acta Mater.* **57** 3704–13
- [6] Fukutomi H and Kamijo T 1985 Grain boundary sliding–migration of aluminium (110) Σ 11(113) symmetric tilt coincidence grain boundary and its interpretation based on the motion of perfect DSC dislocations *Scr. Metall.* **19** 195–7
- [7] Sheikh-Ali A D 1997 On the contribution of extrinsic grain boundary dislocations to grain boundary sliding in bicrystals *Acta Mater.* **45** 3109–14
- [8] Hoagland R G and Kurtz R J 2002 The relation between grain-boundary structure and sliding resistance *Phil. Mag. A* **82** 1073–92
- [9] Hyde B, Farkas D and Caturla M J 2005 Atomistic sliding mechanisms of the $\Sigma = 5$ symmetric tilt grain boundary in bcc iron *Phil. Mag.* **85** 3795–807
- [10] Sansoz F and Molinari J F 2005 Mechanical behavior of Σ tilt grain boundaries in nanoscale Cu and Al: A quasicontinuum study *Acta Mater.* **53** 1931–44
- [11] Cahn J W, Mishin Y and Suzuki A 2006 Coupling grain boundary motion to shear deformation *Acta Mater.* **54** 4953–75
- [12] Mishin Y, Suzuki A, Uberuaga B P and Voter A F 2007 Stick-slip behavior of grain boundaries studied by accelerated molecular dynamics *Phys. Rev. B* **75** 224101
- [13] Ivanov V A and Mishin Y 2008 Dynamics of grain boundary motion coupled to shear deformation: an analytical model and its verification by molecular dynamics *Phys. Rev. B* **78** 064106

- [14] Tschopp M A and McDowell D L 2008 Dislocation nucleation in $\Sigma 3$ asymmetric tilt grain boundaries *Int. J. Plasticity* **24** 191–217
- [15] Hu Q, Li L and Ghoniem N M 2009 Stick-slip dynamics of coherent twin boundaries in copper *Acta Mater.* **57** 4866–73
- [16] Wan L and Wang S Q 2009 Shear response of the $\Sigma 11$, $\{110\}\{131\}$ symmetric tilt grain boundary studied by molecular dynamics *Modelling Simul. Mater. Sci. Eng.* **17** 045008
- [17] Wan L and Wang S 2010 Shear response of the $\Sigma 9(110)\{221\}$ symmetric tilt grain boundary in fcc metals studied by atomistic simulation methods *Phys. Rev.* **82** 214112
- [18] Zhang K, Weertman J R and Eastman J A 2004 The influence of time, temperature, and grain size on indentation creep in high-purity nanocrystalline and ultrafine grain copper *Appl. Phys. Lett.* **85** 5194
- [19] Zhang K, Weertman J R and Eastman J A 2005 Rapid stress-driven grain coarsening in nanocrystalline Cu at ambient and cryogenic temperatures *Appl. Phys. Lett.* **87** 061921
- [20] Jin M, Minor A M, Stach E A and Morris J W 2004 Direct observation of deformation-induced grain growth during nanoindentation of ultrafine-grained Al at room temperature *Acta Mater.* **52** 5381–7
- [21] Jin M, Minor A M and Morris J W 2007 Strain-induced coarsening in nano-grained films *Thin Solid Films* **515** 3202–7
- [22] Gianola D S, Van Petegem S, Legros M, Brandstetter S, Van Swygenhoven H and Hemker K J 2006 Stress-assisted discontinuous grain growth and its effect on the deformation behavior of nanocrystalline aluminum thin films *Acta Mater.* **54** 2253–63
- [23] Gianola D S, Warner D H, Molinari J F and Hemker K J 2006 Increased strain rate sensitivity due to stress-coupled grain growth in nanocrystalline Al *Scr. Mater.* **55** 649–52
- [24] Legros M, Gianola D S and Hemker K J 2008 *In situ* TEM observations of fast grain-boundary motion in stressed nanocrystalline aluminum films *Acta Mater.* **56** 3380–93
- [25] Rupert T J, Gianola D S, Gan Y and Hemker K J 2009 Experimental observations of stress-driven grain boundary migration *Science* **326** 1686–90
- [26] Fang T H, Li W L, Tao N R and Lu K 2011 Revealing extraordinary intrinsic tensile plasticity in gradient nano-grained copper *Sci.* **331** 1587
- [27] Humphreys F J and Hatherly M 2004 *Recrystallization and related annealing phenomena* Pergamon
- [28] Pond R C, Smith D A and Southerden P W J 1978 On the role of grain boundary dislocations in high temperature creep *Phil. Mag. A* **37** 27–40
- [29] King A H and Smith D A 1980 The effects on grain-boundary processes of the steps in the boundary plane associated with the cores of grain-boundary dislocations *Acta Cryst. A* **36** 335–43
- [30] King A H 1982 Step heights associated with grain boundary dislocations in cubic crystals *Acta Metall.* **30** 419–27
- [31] Balluffi R W, Brokman A and King A H 1982 CSL/DSC lattice model for general crystal-crystal boundaries and their line defects *Acta Metall.* **30** 1453–70
- [32] Plimpton S J 1995 Fast parallel algorithms for short-range molecular dynamics *J. Comput. Phys.* **117** 1–19
- [33] Melchionna S, Ciccotti G and Holian B L 1993 Hoover NPT dynamics for systems varying in shape and size *Mol. Phys.* **78** 533–44
- [34] Allen M P and Tildesley D J 1987 *Computer Simulation of Liquids* (Oxford: Clarendon)
- [35] Mishin Y, Mehl M J, Papaconstantopoulos D A, Voter A F and Kress J D 2001 Structural stability and lattice defect in copper: *Ab initio*, tight-binding, and embedded-atom calculations *Phys. Rev. B* **63** 224106
- [36] Mishin Y, Farkas D, Mehl M J and Papaconstantopoulos D A 1999 Interatomic potentials for monoatomic metals from experimental data and *ab initio* calculations *Phys. Rev. B* **59** 3393–407
- [37] Faken D and Jónsson H 1994 Systematic analysis of local atomic structure combined with 3d computer graphics *Comput. Mater. Sci.* **2** 279–86
- [38] Li J 2003 Atomeye: an efficient atomistic configuration viewer *Modelling Simul. Mater. Sci. Eng.* **11** 173–7
- [39] Tschopp M A and McDowell D L 2007 Structures and energies of $\Sigma 3$ asymmetric tilt grain boundaries in copper and aluminum *Phil. Mag.* **87** 3147–73
- [40] Sutton A P and Vitek V 1983 On the structure of tilt grain boundaries in cubic metals: I. Symmetrical tilt boundaries *Phil. Trans. R. Soc. Lond. A* **309** 1–36
- [41] Sutton A P and Vitek V 1983 On the structure of tilt grain boundaries in cubic metals: II. Asymmetrical tilt boundaries *Phil. Trans. R. Soc. Lond. A* **309** 37–54
- [42] Sutton A P and Vitek V 1983 On the structure of tilt grain boundaries in cubic metals: III. Generalizations of the structural study and implications for the properties of grain boundaries *Phil. Trans. R. Soc. Lond. A* **309** 55–68
- [43] Rittner J D and Seidman D N 1996 $\{110\}$ symmetric tilt grain-boundary structures in fcc metals with low stacking-fault energies *Phys. Rev. B* **54** 6999–7015
- [44] Supplementary data. stacks.iop.org/MSMSE/21/055013/mmedia

- [45] Ernst F, Finnis M W, Hofmann D, Muschik T, Schönberger U and Wolf U 1992 Theoretical prediction and direct observation of the 9R structure in Ag *Phys. Rev. Lett.* **69** 620–3
- [46] Campbell G H, Chan D K, Medlin D L, Angelo J E and Carter C B 1996 Dynamic observation of the fcc to 9R shear transformation in a copper $\Sigma = 3$ incoherent twin boundary *Scr. Mater.* **35** 837–42
- [47] Medlin D L, Campbell G H and Carter C B 1998 Stacking defects in the 9R phase at an incoherent twin boundary in copper *Acta Mater.* **46** 5135–42
- [48] Medlin D L, Foiles S M and Cohen D 2001 A dislocation-based description of grain boundary dissociation: application to a $90^\circ \langle 110 \rangle$ tilt boundary in gold *Acta Mater.* **49** 3689–97
- [49] Shimizu F, Ogata S and Li J 2006 Yield point of metallic glass *Acta Mater.* **54** 4293–8
- [50] Forwood C T and Clarebrough L M 1984 Dissociation of asymmetric $\Sigma 9$, $\Sigma 27a$ and $\Sigma 81d \langle 110 \rangle$ tilt boundaries *Acta Metall.* **32** 757–71
- [51] Pond R C and Celotto S 2003 Special interfaces: military transformations *Int. Mater. Rev.* **48** 225–45
- [52] Zhu T, Li J, Samanta A, Leach A and Gall K 2008 Temperature and strain-rate dependence of surface dislocation nucleation *Phys. Rev. Lett.* **100** 25502